Tumor Accumulation of NIR Fluorescent PEG–PLA Nanoparticles: Impact of Particle Size and Human Xenograft Tumor Model

Andreas Schädlich,[†] Henrike Caysa,[†,‡] Thomas Mueller,[‡] Frederike Tenambergen,[†] Cornelia Rose,[§] Achim Göpferich,[§] Judith Kuntsche,[†] and Karsten Mäder[†,*]

[†]Department of Pharmaceutical Technology and Biopharmaceutics, and [‡]Department of Internal Medicine IV, Oncology/Hematology, Martin Luther University Halle-Wittenberg, Wolfgang-Langenbeck-Strasse 4, 06120 Halle (Saale), Germany, and [§]University of Regensburg, Department of Pharmaceutical Technology, Universitätsstrasse 31, 93053 Regensburg, Germany

ABSTRACT Cancer therapies are often terminated due to serious side effects of the drugs. The cause is the nonspecific distribution of chemotherapeutic agents to both cancerous and normal cells. Therefore, drug carriers which deliver their toxic cargo specific to cancer cells are needed. Size is one key parameter for the nanoparticle accumulation in tumor tissues. In the present study the influence of the size of biodegradable nanoparticles was investigated in detail, combining *in vivo* and *ex vivo* analysis with comprehensive particle size characterizations. Polyethylene glycol–polyesters poly(lactide) block polymers were synthesized and used for the production of three defined, stable, and nontoxic near-infrared (NIR) dye-loaded nanoparticle batches. Size analysis based on asymmetrical field flow field fractionation coupled with multiangle laser light scattering and photon correlation spectroscopy (PCS) revealed narrow size distribution and permitted accurate size evaluations. Furthermore, this study demonstrates the constraints of particle size data only obtained by PCS. By the multispectral analysis of the Maestro *in vivo* imaging system the *in vivo* fate of the nanoparticles next to their accumulation in special red fluorescent DsRed2 expressing HT29 xenografts could be followed. This simultaneous imaging in addition to confocal microscopy studies revealed information about the accumulation characteristics of nanoparticles inside the tumor tissues. This knowledge was further combined with extended size-dependent fluorescence imaging studies at two different xenograft tumor types, the HT29 (colorectal carcinoma) and the A2780 (ovarian carcinoma) cell lines. The combination of two different size measurement methods allowed the characterization of the dependence of nanoparticle accumulation in the tumor on even rather small differences in the nanoparticle size. While two nanoparticle batches (111 and 141 nm in diameter) accumulated efficiently in the human xenograft tumor tissue, the slightly bigger nanoparticles (diameter 166 nm) were rapidly eliminated by the liver.

KEYWORDS: *in vivo* imaging · fluorescence imaging · AF4 · PEG–PLA · nanoparticle · HT29 · A2780

Unfortunately, a high percentage of potent drug candidates for anticancer therapy are poorly soluble in water.[1,2] Many of them possess a polycyclic structure which enhances the ability of the molecules to reach cellular targets.[3] Owing to their hydrophobic characteristics many of these therapeutic agents never enter the formulation development stage.[1] This remains one of the main challenges in future anticancer chemotherapy. Nanoparticles with a hydrophobic matrix provide an excellent possibility for the formulation of such poorly water-soluble drugs. The biodegradable and biocompatible polyesters poly(lactide) (PLA) and poly(lactide-co-glycolide) (PLGA) are frequently used for this purpose and are approved in several market products for parenteral application by the FDA.[4] PLA is more hydrophobic as compared to PLGA. Therefore, PLA nanoparticles can homogeneously incorporate very lipophilic drugs in their core. After intravenous (i.v.) application and possible accumulation into tumor tissue the slow degradation of PLA[5,6] provides a continuous release of the drug at the place of its action. Such nanoparticles thus present an interesting approach for a convenient therapy with extended drug administrations. However, the nanoparticles have to reach and accumulate in tumor tissues where the drug is needed. Both steps, transport *via* the bloodstream as well as tumor enrichment are triggered by two main parameters, the particle size and the surface properties of the nanoparticles.

It is well established that flexible hydrophilic surfaces like polyethylene glycol (PEG) have the ability to extend circulation time and retention half-life of nanoparticles as they reduce opsonisation and the subsequent clearance by the mononuclear phagocytic system (MPS) also known as reticuloendothelial system (RES). The RES has been shown to be the major barrier for an effective tumor targeting using nanoparticles.[7] Thereby, mainly the Kupffer cells of the liver

* Address correspondence to karsten.maeder@pharmazie.uni-halle.de.

Received for review July 14, 2011 and accepted October 3, 2011.

Published online October 03, 2011
10.1021/nn2026353

as well as the macrophages of the spleen have been identified to be responsible for the rapid clearance of nanocarriers from the bloodstream.[7,8] Tumor tissue is often characterized by a leaky vasculature with an enhanced permeability.[7,9] Intravenously injected nanoparticles can accumulate by passive diffusion due to this hyper-permeable tumor vasculature. This retention of nanoparticles in the tumor tissue is called EPR (enhanced permeability and retention) effect.[10] Individual molecules like drugs and dyes are transported through the bloodstream for only a few minutes up to 1 h until they are eliminated rapidly. In contrast, properly designed, nanoparticles can reach much longer circulation times and have the ability to be retained in tumor tissues due to the EPR effect. It has been shown that the upper size limit for extravasation into solid tumors is about 400 nm.[11] Other groups showed that particles with diameters <200 nm accumulate even more effectively than bigger ones.[9,12,13] This can be explained by an increased nanoparticle uptake by the RES in the size range between 150 and 300 nm.[14] A lower size limit based on size is difficult to define due to further influencing parameters like structure, surface charge, and molecular-flexibility.[15] Studies have shown that the size limit for renal excretion of proteins and water-soluble polymers is approximately 45 kDa (hydrodynamic diameters <8 nm), depending on the particle size, shape, density, and the surface charge.[15−18] It is furthermore known, that also liposomes which are smaller than 70 nm are faster cleared from the bloodstream than larger ones.[19,20] This is the effect of extravasation and accumulation in the parenchymal cells of the liver.[20] On the basis of this knowledge and of other reports, the optimum nanoparticle size for tumor accumulation is between about 70 and 200 nm.[21] This rather narrow size range clarifies the necessity of the preparation of nanoparticle formulations with well-defined and characterized sizes and sufficiently narrow size distributions. Only some few publications discuss nanoparticle-dependent tumor accumulation and *in vivo* biodistribution, however, based on particle batches with polydispersity indexes (PDI) between 0.2 and 0.5.[22,23] Because of the broad particle size distribution in these studies, information about the *in vivo* fate can only be drawn with care. This again underlines the necessity to control the size of the nanoparticles during preparation. In addition, reliable and appropriate size determinations using different size measurement techniques are necessary as the basis for meaningful interpretation of *in vivo* data.[24]

The aim of the present work was to investigate the *in vivo* fate and tumor accumulation of three PEG_2-PLA_{20} or PEG_2PLA_{40} (numbers in kDa) nanoparticle formulations with different and defined sizes. Storage stability, homogeneity after redispersing, and sufficient stability in aqueous media as well as high biocompatibility were already established, and the results evidenced the high potential of these nanoparticles as drug delivery systems.[25] In addition, nanoparticle sizes were studied in detail using asymmetrical field flow field fractionation (AF4) coupled with multiangle laser light scattering (MALLS) and photon correlation spectroscopy (PCS). These size evaluations were the main requirement to correlate the influence of particle size on the *in vivo* distribution, studied by near-infrared (NIR) fluorescence imaging.[25] This imaging technique provided a noninvasive monitoring modality with high temporal resolution also in deep tissues.[26] Fluorescence imaging, especially the Maestro *in vivo* imaging system allowed the detection of multispectral emission curves and also the exclusion of the autofluorescence from the mice.[25,27] Hence, contemporaneous imaging analysis of fluorescent tumors, dyed nanoparticles and autofluorescence of the mice was possible.

In the present study, tumor accumulation of PEG−PLA nanoparticles differing in size was evaluated on two different xenograft tumor types simultaneously to improve the understanding of the *in vivo* nanoparticle tumor targeting capacity. Xenograft tumors derived from the HT29 colon carcinoma cell line and the A2780 ovarian carcinoma cell line were selected due to their differences in structural shape and growth.

To the best of our knowledge, it is the first time that the influence of size of narrow distributed nanoparticle batches were studied in detail using AF4/MALLS as well as PCS and combined with extensive biodistribution studies. The results of this study provide information about the influence of the particle size on the *in vivo* fate and tumor accumulation behavior of PEG−PLA nanoparticles up to the cellular level. This study serves as the basis for further nanoparticle applications to enhance the therapeutic activity and safety of chemotherapeutic agents.

RESULTS AND DISCUSSION

Nanoparticle Preparation. By variation of the polymer concentration in a fixed volume of the organic solvent, the particle size of the nanoparticles can be controlled. Higher polymer concentrations lead to increased particle sizes. On the other hand, the ratio of the external aqueous phase or the amount of the polymer solution (at fixed polymer concentration) had nearly no effect on the size of the produced nanoparticles.[28] On the basis of this knowledge, different amounts of PEG−PLA were used to produce three batches of DiR-loaded nanoparticles with different sizes (Table 1). One unloaded batch was produced for extended size characterizations (batch D). Previous studies on the physical stability and polymer degradation attested the nanoparticles to be stable in the dried state for more than 6 months. The nanoparticles were even

TABLE 1. Nanoparticle Compositions and Particle Sizes of Freshly Dissolved Nanoparticle Batches

batch polymer[a]	A, PEG_2PLA_{20}	B, PEG_2PLA_{40}	C, PEG_2PLA_{40}[d]
DiR loading[b]	0.5%	1%	1%
polymer concentration[c]	0.75%	1%	2%
PCS, *z*-average in nm (PDI)	111 ± 2 (0.16)	141 ± 1 (0.13)	166 ± 2 (0.13)
MALLS D10 (nm)	36 ± 2	40 ± 1	48 ± 10
MALLS D50 (nm)	43 ± 2	64 ± 1	99 ± 4
MALLS D90 (nm)	80 ± 3	153 ± 1	230 ± 2
fluorescence intensity	~ 32	~ 100	~ 76

[a] The number 2, 20, and 40 refers to the molar mass of the polymer block (kDa). [b] Dye loading in percent related to the polymer amount. [c] Polymer concentration in percent related to the organic solvent. [d] Data is based on previously shown results.[25]

stable in aqueous dispersion for up to 3 months when stored in the refrigerator at about 5 °C, and no agglomeration or degradation was observed.[25] These findings are in good accordance with literature data.[29,30]

Physicochemical Properties. *Fluorescence Spectroscopy.* Fluorescence intensities of the different nanoparticle batches are shown in Table 1. Lowest intensities were measured for batch A nanoparticles due to the lower DiR-load of these nanoparticles. Batch B showed highest fluorescence intensities indicating high incorporated dye amounts. The intensity of batch C was in between where the dye loading was decreased due to the higher amount of polymer.

Photon Correlation Spectroscopy (PCS). The hydrodynamic mean particle diameters (*z*-averages) are presented in Table 1. The results confirmed the production of nanoparticles with different sizes. The size range was between 111 nm (batch A) and 166 nm (batch C), hence within the size range which is reported to be ideal for cancer treatment (70−200 nm).[21] All PDI values were between 0.13 and 0.16 indicating an overall narrow particle size distribution.

Asymmetrical Flow Field Flow Fractionation (AF4). AF4/MALLS measurements allowed an accurate determination of size distributions due to the fractionation step prior to size determination.[31,32] The calculated D10, D50, and D90 diameters of all three batches are shown in Table 1. The D50-diameters (median) were considerably smaller compared to the PCS *z*-averages. This was caused by geometrical mass weighed particle sizing in AF4 measurement which reduced the influence of the water shell and the presence of minor amounts of larger particles in all batches. All three nanoparticle batches had small fractions of larger particles (>200 nm) but no particles with diameters larger than 600 nm could be detected.

Nevertheless, the LS detector signals over the whole elution time as well as the corresponding cumulative mass distributions (Figure 1) confirmed the overall narrow size distribution of the nanoparticle batches. The analysis of batch A indicated that the predominant fraction of nanoparticles was in the size

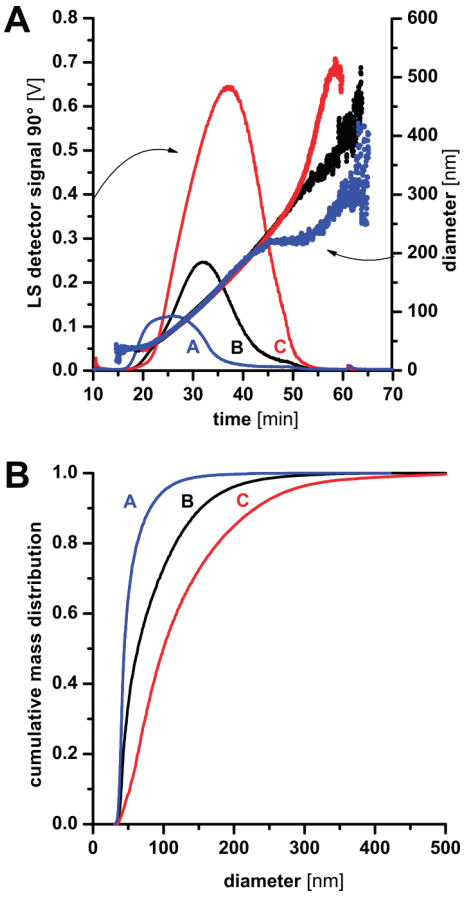

Figure 1. (A) AF4/MALLS elution profiles (light scattering signal at 90°) and corresponding diameters of the nanoparticle dispersions (arrows indicate the assignment). (B) Cumulative mass weighted size distributions of PEG−PLA nanoparticles, determined by AF4/MALLS.

range between 36 and 80 nm. Only less than 10% were larger than 100 nm (Table 1). Size distribution was broadest for batch C. The amount of nanoparticles which was smaller than 48 nm was similar to that with sizes larger than 230 nm. The results indicated that PCS *z*-averages are mainly influenced by larger particles. This underlined the advantages of AF4 to get more detailed information of the nanoparticle size distribution which has a major influence to possible *in vivo* behavior.

Nanoparticle Stability in FBS and PBS Containing Media. The PCS and AF4 measurements were extended to investigate the influence of physiological conditions to the particle size distribution (Table 2). The *z*-average in water was determined to be 112 nm with a PDI of 0.08 indicating an even narrower distribution than that of the loaded nanoparticles. Consequently, the D50 value of 100 nm based on the AF4 results was comparable to the PCS result. The difference of 12 nm can be attributed to the water binding between the PEG chains, which influence the movement of the particles in the PCS measurement. The addition of PBS had no influence on the *z*-average although the

TABLE 2. Particle Size of PEG_2PLA_{40} Nanoparticles in Different Dispersing Media

	PCS, *z*-average in nm (PDI)	MALLS D10 in nm	MALLS D50 in nm	MALLS D90 in nm
water	112.0 (0.08)	69	100	150
water (10% PBS)[a]	112.3 (0.10)			
water (10% FBS)[a]	91.1 (0.29)	71	101	151
water (10% FBS, 10% PBS)[a]	90.8 (0.30)			
water (50% FBS)[a]		68	101	151

[a] Particle sizes were determined 24 h after incubation.

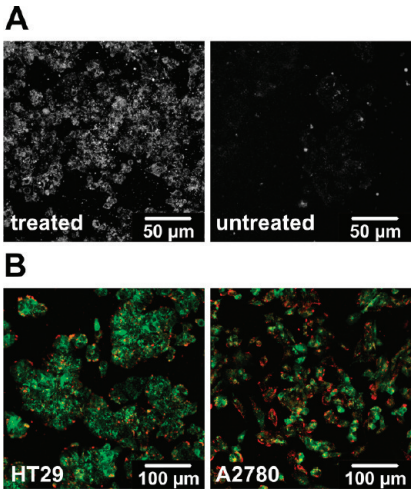

Figure 2. (A) Grayscale intensity confocal microscopic images of HT29 tumor cells (incubated with batch A and untreated). (B) Carcinoma cells, incubated with batch A nanoparticles (red) and stained by membrane dye DiO (green).

PDI was slightly increased (0.10). Measurements in FBS containing media yielded in *z*-averages of 91.1 and 90.8 nm with PDI values of 0.29 and 0.30 (Table 2). The increase of the PDI values and the reduced particle size is caused by the proteins in the serum (mainly albumin, high-/ and low-density lipoproteins) which influenced the PCS measurements. This is not the case in the AF4 measurements where the sample is fractionized prior to size determination. The measured D10, D50, and D90 values in FBS containing media are in the same range as in measurements of the samples dispersed in pure water. The results indicate that the nanoparticles are stable also in physiological media.

Cellular Confocal Microscopy Studies. On the basis of reported size-dependent nanoparticle adsorption and uptake by cells,[33] smaller particles should be more suitable to study the nanoparticle behavior on the cellular level. Therefore, cell experiments were performed using the smallest nanoparticles (batch A). First tests were carried out with unstained HT29 cells, the same cell line as used for further *in vivo* experiments. The images of treated and untreated cells are given exemplarily as grayscale intensity images in Figure 2A with clear differences in the fluorescence intensities. The results indicate that the nanoparticles have the ability to bind to or to accumulate in the cells. On the basis of these experiments, the tests were repeated using both A2780 cells, the second cell line used *in vivo*, and HT29 cells. Cell membranes were stained with DiO for better localization of fluorescent nanoparticles. Overall, the results indicate that the nanoparticles were mainly bounded to the cell membranes in both cell lines but with a higher association tendency to A2780 tumor cells (Figure 2B). This might be caused by the PEG shell which inhibits the nanoparticle uptake into the cells.[34] But it has to be kept in mind that PEG is necessary to circumvent nanoparticle recognition by the RES. If they are fast eliminated by the liver they will not reach tumor tissues and *in vitro* observed nanoparticle uptake will fail *in vivo*. But even nanoparticles, which stick on the surface, will slowly be eroded and degraded. Thereby, the dyes or drugs will be released and diffuse into the cells effectively.

***In Vivo* Accumulation Studies in DsRed2 Fluorescent HT29 Tumors.** Nanoparticle accumulation was studied in male nude mice bearing two subcutaneous (s.c.) HT29 xenograft tumors, one on each flank. For clear visualization of nanoparticle accumulation in the tumor tissue and normal nanoparticle distribution within the body, DsRed2 expressing HT29 cells were used. This allowed multispectral *in vivo* imaging of dyed NIR nanoparticles (red) and the fluorescent tumor cells (green) simultaneously (Figure 3A). At 10 min after i.v. application of NIR fluorescent nanoparticles high fluorescence intensities were detected in the s.c. blood vessels in the abdominal area. Also the blood vessels above both tumor grafts (green fluorescence) were well visible. The intensity of the circulating particles decreased continuously with time after injection and were detectable in the blood vessels for about 6 h. Afterward the intensity fell below the detection limit of the fluorescence imager.[25]

The scaled intensity images (Figure 3B) were obtained by using the "compare imaging" function of the extracted DiR signal. This allowed time dependent visualization of nanoparticle accumulation in tumor tissues. Different measurement conditions like varying exposure times were recomputed by the software and all four images were displayed in relation to each other.

The big blood vessels under the skin were well visible within the first minutes after injection (Figure 3B). Already 3 h later there was a clear accumulation in the area of the tumor accompanied by a simultaneously decreased intensity in other parts of the body. The enrichment within the HT29 tumors increased distinctly up to 24 h (Figure 3B). This was probably caused by the EPR effect by what the passive accumulation of nanocarriers occurs after a single application during the first 24 h.[35,36] After 48 h the DiR intensity in the tumor decreased continuously but remained visible

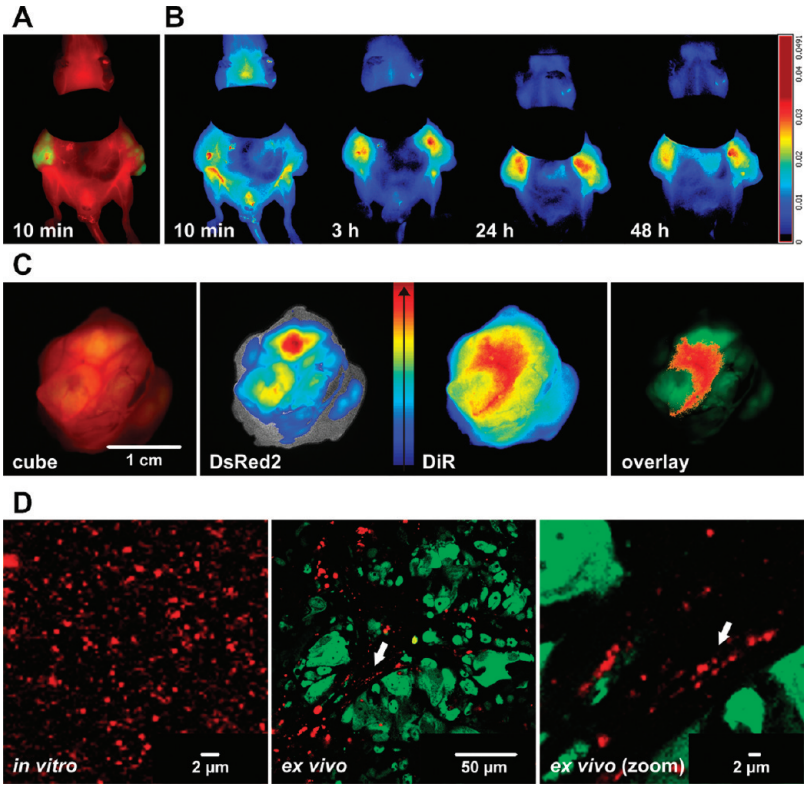

Figure 3. (A) Unmixed fluorescence image (DiR signal = red, DsRed2 = green) of a mouse bearing 2 DsRed2 expressing HT29 xenograft tumors (left and right). (B) Time-dependent intensity images (isolated DiR signal) of the same mouse. The area of the liver was masked. (C) *Ex vivo* fluorescence images of a DsRed2 fluorescent HT29 colon carcinoma (from left to right: raw image, intensity weighted jet color image of the extracted DsRed2 and DiR signal, overlay of high intensity DiR parts and in green displayed fluorescent DsRed2 areas). (D) Confocal microscopic images: *in vitro* DiR nanoparticle dispersion and *ex vivo* images, DsRed2 tumor cells in green with accumulated DiR nanoparticles in red (same areas are marked by an arrow).

over several days as shown exemplarily in Figure 3B. This result is in agreement with the understanding of the EPR effect.[10] Owing to polymer degradation at 37 °C which is reported to take *in vitro* more than 1 month[29,30] we expect a continued long-term release of the dye from the nanoparticles.

***Ex Vivo* Accumulation Studies in DsRed2 Fluorescent HT29 Tumors.** A DsRed2 fluorescent tumor bearing mouse was sacrificed 48 h after nanoparticle injection (Figure 3B). The tumor was imaged *ex vivo* using the Maestro (Figure 3C). Analyzing the cube to assign DiR and DsRed2 signals allowed the generation of respective corresponding jet color intensity images. The DsRed2 image (Figure 3C) revealed clusters with high fluorescence intensity of DsRed2 expressed cell clusters. DiR jet color image in Figure 3C illustrated the fluorescent areas where DiR nanoparticles accumulated. Highest concentrations were located between DsRed2 expressing cells. This was confirmed by the overlay image (Figure 3C). The highest threshold values of the DiR signal were displayed red, and this information was afterward overlaid on the green displayed DsRed2 areas.

After *ex vivo* imaging a sliced tumor part was analyzed by confocal microscopy. By this, the detection of NIR fluorescent nanoparticles in addition to the DsRed2 expressing tumor cells was possible. Figure 3D shows the plain-imaged nanoparticle suspension for comparison. The red-appearing DiR-loaded nanoparticles were homogeneously distributed and scaled in the nanometer size range. Compared to the size results obtained by PCS and AF4/MALLS, the particles appeared bigger due to also laterally emitted fluorescence light. Examination of the sliced tumor tissue (Figure 3D) allowed visualization of the PEG–PLA nanoparticles (red spots) between the xenograft tumor cells (green). Most nanoparticles were located in non-DsRed2 fluorescent, channel-like areas. These consist either of necrotic tumor tissue or of nonfluorescent mouse cells. On the basis of additional performed hematoxylin and eosin (H&E) analyses, an accumulation of nanoparticles mainly in necrotic/fibrotic tumor tissue was proven.

***In Vivo* Fluorescence Imaging Studies.** Nonfluorescent HT29 and A2780 cell lines were used as xenograft models to evaluate tumor accumulation dependent on the nanoparticle size. The HT29 tumors are characterized by their bright and firm shape; they grow slower than A2780 tumors and generally contain large central necrotic/fibrotic areas which are surrounded by peripherally arranged vital tumor cells.[37] The A2780 tumors grow faster and are highly vascularized. Their

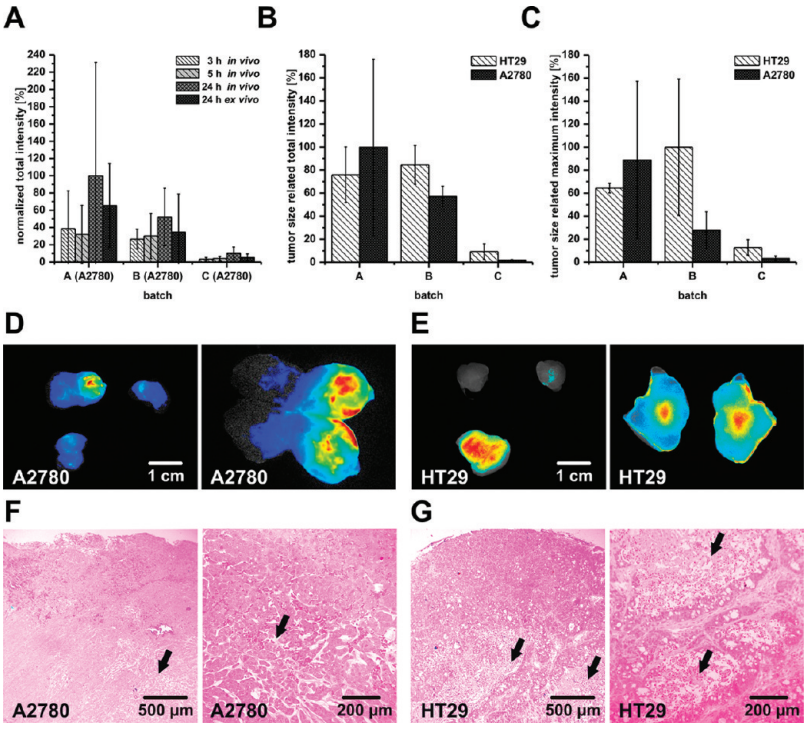

Figure 4. Normalized total fluorescence intensity amounts (A, B) and maximum intensities (C). (A) Time-dependent nanoparticle accumulation in A2780 tumors, *in vivo* measured compared to 24 *ex vivo* results. (B and C) Tumor size related fluorescence intensities of HT29 and A2780 tumor accumulation values, 24 h after i.v. injection, measured *ex vivo* (SD, $n = 3$). (D and E) *Ex vivo* fluorescence images of excised (left) and sliced (right) xenograft tumors (group A, 24 h after i.v. injection). (F and G) Light microscopic images of excised and sliced xenograft tumor tissues (H&E stained). Arrows point to blood vessels (F) and central necrotic areas (G).

blue color attests a high perfusion and vascular permeability which is more than 4 times higher than that in neighboring tissues.[38] Owing to the smaller amount of connective tissue, A2780 tumors are more soft compared to HT29 tumors.

For direct comparison, both of these xenograft tumors were established in the same mouse, one to the right and to the other to the left side. The A2780, known as a fast growing tumor, reached in all groups average tumor sizes between 1.25 and 2.25 cm^3. They were 3−6 fold bigger than the HT29 ones (0.3−0.5 cm^3) and showed larger size variations within the respective group. All mice were imaged for 24 h after nanoparticle injection of batches A, B, and C (Table 1). The resulting *in vivo* images yielded overall similar nanoparticle distributions as shown in Figure 3A,B. NIR nanoparticles accumulated slowly but continuously in the tumor during the first 24 h after injection. Nanoparticle tumor accumulation was clearly detectable *in vivo* in more than 80% of the mice. However, pharmacokinetic data and tumor enrichment differences between all three nanoparticle batches could not be visualized due to the limited resolution of the fluorescence images.

***Ex Vivo* Fluorescence Imaging Studies.** The distribution pattern inside both tumor models was further investigated by the comparison of fluorescence images of complete and sliced tumor tissues. The results of group A are exemplarily shown in Figure 4D,E. Nanoparticles were highly enriched in all three A2780 tumors (Figure 4 D). In contrast the smaller HT29 tumors showed no or only slight fluorescence, whereas the bigger one was highly fluorescent (Figure 4 E). After cutting the HT29 tumor into two pieces, inhomogeneous fluorescence of accumulated nanoparticles was visible. Two areas with highest fluorescence intensity could be identified: the boundary and the central area. On the basis of Figure 4D an irregular distributed nanoparticle accumulation in the A2780 tumor tissue can be assumed. Different inner and surface parts are dark-red. In contrast there are large areas appearing dark-blue with only low fluorescence intensity, indicating areas with less accumulated nanoparticles. Dark-red and dark-blue areas as found in the A2780 tissue (Figure 4D) indicating only very high or minor nanoparticle concentrations could not be seen in the HT29 tumors (Figure 4E). This confirmed a more homogeneous nanoparticle distribution throughout the tumor. The low interstitial pressure in parts of the HT29 tumor tissue causes that after extravasation, the nanoparticles diffuse and accumulate in the tumor center (Figure 4E). As it is visible in the H&E stained light microscopic images shown in Figure 4G, this is an area with low central microvessel densities but with central fibrotic and or necrotic areas which is in accordance with literature.[37,39,40] Jain *et al.* characterized the

TABLE 3. Normalized Total and Maximum Intensities of Different Mouse Organs and Tissues, Measured *ex Vivo*

	total intensity signal						maximum intensity signal					
batch:	A		B		C		A		B		C	
gender:	m[a]	f[b]	m[a]	f[b]	m[a]	f[b,c]	m[a]	f[b]	m[a]	f[b]	m[a]	f[b,c]
liver	39.8	45.0	34.8	37.4	100.0	88.8	53.4	47.4	56.2	29.6	100.0	89.0
spleen	8.8	9.3	9.0	0.5	12.4	15.2	34.9	25.4	27.4	4.8	41.8	37.9
gall bladder		0.1				0.4	1.1	11.2	5.5	4.2	2.4	33.2
intestine		1.5	1.2	0.5	1.2	4.5	5.3	7.9	11.6	6.2	9.0	14.2
kidney		0.4	0.2	0.1		0.1	2.1	4.7	4.6	1.0	4.8	7.3
lung		0.1	0.2		0.1	0.1	22.5	17.8	4.9	0.5	4.3	5.6
fat			0.1				2.5	4.9	2.3	0.4	2.1	9.6
heart		1.5	1.2	0.5	1.2	4.5	5.3	7.9	11.6	6.2	9.0	14.2

[a] Data in percent based on three male mice per nanoparticle batch, 24 h after injection. [b] Data in percent based on four female mice per nanoparticle batch, 24 h after injection. [c] Data are based on previously shown results.[25]

necrotic tissues as regions with less blood vessels and low blood flows.[41] Immediately after i.v. injection, the nanoparticles are transported to perfused regions. Owing to the low interstitial pressure in parts of the tumor, tissue extravasation of nanoparticles is possible. Afterward they can diffuse to necrotic areas where they accumulate. Thus loaded nanoparticles would allow high intratumoral drug concentrations, and the anticancer therapy could start from the tumor center. The low interstitial pressure would also explain that no size dependent differences between the accumulation of batch A and B nanoparticles were found within HT29 tumor tissues. A2780 tumor tissues are better supplied with blood (Figure 4 F). Numerous blind ends, occlusions, and wall defects of the tumor blood vessels promote nanoparticle accumulation.[42]

***Ex Vivo* Biodistribution Analysis.** The degree of nanoparticle accumulation in different organs and tissues based on *ex vivo* fluorescence measurements is shown as normalized total and maximum intensities in Table 3. Owing to the linear relationship between exposure time and fluorescence intensity, the Maestro software allows the calculation of exposure-time independent total and maximum intensities. By a previously described calculation method, different nanoparticle batches with consequently varying DiR concentration could be compared.[25]

Measured total intensities as the sum of all pixels of the respective organ and tissue are shown in the left rows of Table 3. It is visible that highest intensities were found in both organs of the RES, the liver, and the spleen. Batch A and B nanoparticles accumulated in similar amounts in the liver. The smaller size and the higher PLA/PEG ratio of batch A nanoparticles (PLA with a molecular weight of 20 kDa and consequently a higher amount of PEG) compared to batch B had no positive effect to reduce liver accumulation. This might be explained by an optimum size range for both batches and a completely PEG covered surface already in the case of batch B nanoparticles with an PLA:PEG ratio of 20:1 which cannot be improved by higher PEG amounts. However, for batch C nanoparticles with the largest mean size, liver accumulation was clearly highest. The larger fraction of nanoparticles with bigger size (Figure 1) yielded in a nearly double amount of nanoparticles in the liver. This observation is in agreement with other published data where an increased nanoparticle uptake by the RES was found in size ranges between 150 and 300 nm.[14]

The intensity levels of all other organs and tissues were in the single-digit range. Nearly the same values were obtained for the male and the female mouse group. This underlines the reproducibility of our *in vivo* studies. The corresponding maximum intensity signals are also given in Table 3 (right rows). The maximum intensities allow a restricted comparison of organs and tissues varying in size although the errors of the measurement especially at the lower limit highly increase. Liver and spleen have comparable optical properties. Therefore, the maximum intensity allows a comparison of the accumulation rate between the bigger liver and the much smaller spleen. The results indicate a slightly decreased liver and an increased spleen uptake for the smaller nanoparticles. The maximum intensity results further confirm that no specific accumulation occurred in the kidneys, the lung, the fat, and the heart. An accumulation of nanoparticles based on higher maximum fluorescence intensities, measured for batch A in the lung and for batch B and C in the heart, could not be confirmed in the fluorescence images as fundamental accumulation. The slightly higher intensity level in the gall bladder and the intestine indicate the renal excretion of the particles, which was visually confirmed earlier.[25]

***In Vivo* and *ex Vivo* Tumor Accumulation Analysis.** Normalized total and maximum tumor intensities based on *in vivo* and *ex vivo* imaging data for all three batches are shown in Figure 4A,B. The calculated total intensities of

the A2780 tumors based on *in vivo* and *ex vivo* measurements are shown in Figure 4A. It is visible that the total intensity remained constant between 3 and 5 h and was doubled after 24 h. This might be explained by the long circulation time of the nanoparticles. Blood vessels were detectable up to 6 h, still indicating circulating nanoparticles. During the next hours an increasing number of nanoparticles accumulated in the tumor and those still circulating were continuously removed by the RES. The *ex vivo* signals, measured 24 h after injection are in good agreement with the *in vivo* obtained total intensities (Figure 4A). The decreased level of the total intensity measured *ex vivo* is the result of the slightly imprecise tumor definition within the ROI analysis of the *in vivo* cube file. The degrees of nanoparticle accumulation in A2780 and HT29 tumor tissues based on *ex vivo* data are shown in Figure 4B,C. To allow comparison between the larger A2780 and the smaller HT29 tumors both the normalized total and the normalized maximum intensities were divided by the respective *ex vivo* determined tumor volume. It is clearly visible that nearly the same tendencies were obtained for both normalized total and normalized maximum intensities. Lowest tumor accumulation generally was found for batch C nanoparticles. This can be explained by the above-discussed efficient elimination of the particles from the bloodstream by the RES (Table 3). For the A2780 ovarian carcinoma xenograft a strong size dependence of tumor accumulation was found (Figure 4B): Batch A nanoparticles with the smallest size (*z*-average = 111 nm, D90 = 80 nm) showed ~50-fold higher total intensities compared to the total intensities measured for batch C and ~2-fold compared to that of batch B. Examining the normalized maximum intensity of the A2780 tumor (Figure 4C), even a ~27-fold increase of the intensity between batch C and A was observed. The size difference between both batches A and B of 30 nm based on the *z*-average values (PCS measurements) and of 70 nm based on the D90 diameter results (AF4/MALLS analysis) resulted in a more than doubled enrichment for the smaller nanoparticles (Figure 4B,C). Within comparable liver accumulations between batch A and B nanoparticles we expected that the smaller size of batch A had a positive tumor-enhancing effect. Owing to high perfusion and vascular permeability of the A2780 ovarian carcinoma, this might be based on the EPR effect which is known to be highly size dependent.

In contrast to the A2780 tumors, the highest accumulation in the HT29 tumor was detected for the medium-sized nanoparticles (batch B, *z*-average = 141 nm, D90 = 153 nm). Batch A nanoparticles showed comparable but slightly decreased accumulation rates. Batch C (*z*-average = 166 nm, D90 = 230 nm) appeared to be not suitable for tumor accumulation. The tumor-size-related total and maximum intensity of batch C were 5- to 9-fold reduced compared to the values of the other two batches. Based on the tumor size related calculations nearly the same normalized maximum and total intensity values (Figure 4B,C) indicate for HT29 and A2780 a homogeneous tumor accumulation.

CONCLUSION

In the present study, we investigated the size-dependent *in vivo* fate of PEG–PLA nanoparticle batches with different but well-defined sizes. Therefore, detailed particle size characterizations prior to the *in vivo* studies were carried out. We could show that nanoparticle batches with different sizes (*z*-averages between 111 and 166 nm in our study) within the optimum size range for tumor accumulation[21] can be produced. Noninvasive multispectral NIR fluorescence imaging studies allowed nanoparticle detection just after injection up to 48 h. Combining DsRed2 expressing HT29 tumor cells with *in vivo* fate studies permitted nanoparticle tracking simultaneously next to tumor visualization from *in vivo* to *ex vivo*, up to cellular ranges. The confocal microscopic pictures confirmed the *ex vivo* imaging results where particles were located between fluorescent, DsRed2 expressing cells.

In vivo studies with HT29 and A2780 tumor bearing mice showed that nanoparticles accumulated in both tumors. Interestingly, the *ex vivo* studies furthermore demonstrated that the accumulation pattern mainly differs between both used tumor models. In the HT29 tumor tissue nanoparticles enriched in the tumor center primarily, whereas A2780 showed no centralized nanoparticle accumulation. Furthermore, highest tumor enrichments were found with batch A nanoparticles for the A2780 and comparable accumulations for batch A and B nanoparticles in the case of HT29 tumors. This points to the fact that the accumulation in centralized necrotic fields (HT29) is not as size dependent as it is for vascular permeation (A2780). *Ex vivo* viscera distribution studies showed distinct differences between the larger particles of batch C compared to those of batches A and B. The increased particle size yielded in high uptake rates by the RES and therewith to very low tumor accumulations. The presented results showed impressively the size-dependent *in vivo* behavior of produced nanocarriers. Slight differences between the *z*-averages of ~30 nm (between batch A and B) and of ~20 nm (between batch B and C) with—compared to literature—rather low PDI values (between 0.13 and 0.16) resulted in strongly different *in vivo* results. The addition of AF4/MALLS as a further particle size measurement method attested that all three nanoparticle batches varied more in size than PCS data would let expect. Whereas D50 values yielded same size intervals as measured within the PCS results (~20 and ~30 nm), D90 results attested size differences of ~70 nm (between batches A and B) and

~80 nm (between batches B and C). On the basis of these results, the combination of extended accurate size determinations with *in vivo* fluorescence imaging technique appears to be a very promising approach to study the size-dependent fate and tumor accumulation of nanoparticles.

MATERIALS AND METHODS

Materials. 3,6-Dimethyl-1,4-dioxan (D,L-lactide), poly(ethylene glycol) monomethyl ether (mPEG2000; MW = 2000 Da), stannous 2-ethylhexanoate (>95%), phosphate buffered saline (PBS) buffer solution, and sorbitol were obtained from Sigma Aldrich, Germany. Sucrose was obtained from Merck KGaA, Germany, poloxamer 188 (Pluronic F68) from Riedel-de Haën, Germany, and paraffin as well as formalin (≥35%) from Carl Roth, Germany. The fluorescence dye 1,1′-dioctadecyl-3,3,3′,3′-tetramethylindotricarbocyanine iodide (DiR), Dulbecco's phosphate buffered saline (PBS) and the Vybrant DiO cell-labeling solution (DiO) were purchased from Invitrogen, Germany. RPMI-1640 medium, 1% streptomycin/penicillin solution, and fetal bovine serum (FBS) were provided from PAA, Austria, and 10% fetal bovine serum came from Biochrom AG, Germany. Polystyrene standard nanoparticles were obtained from Duke Scientific, United States (50, 100, 200 nm), and from Beckman Coulter, Germany (300 nm). All other substances and solvents were used as received.

Synthesis and Preparation of PEG−PLA Nanoparticles. The synthesis of the diblock copolymers PEG_2PLA_{20} and PEG_2PLA_{40} followed a previously established procedure.[25] The numbers refer to the molecular weight of the respective polymer block (in kDa). A nanoprecipitation method was used for the nanoparticle preparation as described earlier.[25] In brief, a solution containing different amounts of polymer in 5 mL of chloroform and the NIR dye DIR (for batches A−C) was dropwise added to 40 mL of an aqueous solution containing 0.25% (w/v) poloxamer 188. Thereafter, the organic solvent was removed by evaporation under stirring the dispersion at room temperature. The nanoparticles were then collected by centrifugation, washed with purified water, resuspended in 5% sucrose solutions and subsequently freeze-dried.

Physicochemical Nanoparticle Characterization. *Fluorescence Spectroscopy.* Fluorescence spectra (775−900 nm) of the nanoparticles redispersed in water (nanoparticle concentration 0.23 mg/mL) were recorded using a LS 55 spectrophotometer (PerkinElmer, United States) equipped with a red-sensitive R928 photomultiplier (750 V), following excitation with 750 nm. The measured intensities were subsequently normalized to the particle concentration.

Photon Correlation Spectroscopy (PCS). For PCS measurements, all three DiR-loaded nanoparticle batches (batch A−C, Table 1) as well as a dye free PEG_2PLA_{40} batch (batch D) were diluted with purified, filtered (0.2 μm) water to reach a nanoparticle concentration of 0.1 mg/mL. The unloaded nanoparticles were furthermore dispersed in purified water containing 10% PBS buffer, 10% FBS, and 10% of both, PBS and FBS, respectively. The measurements were carried out with a high performance particle sizer (HPPS, Malvern Instruments, Germany). The samples were measured four times in the backscattering mode (173°) at room temperature (25 °C) with 12−16 runs over 10 s each at a fixed measurement position in the middle of the cuvette. Samples in PBS and FBS were measured after 24 h of storage to detect possible interactions between the nanoparticles themselves or between the nanoparticles and serum components. The mean particle size (z-average) and the PDI were determined by the instruments cumulant analysis software (version 4.20), $n = 4$ for batches A−C and $n = 3$ for batch D.

Asymmetrical Field Flow Field Fractionation (AF4). Particle size distributions of the nanoparticles were measured by AF4 (Eclipse, Wyatt Technology Europe, Germany) coupled with a MALLS detector (DAWN EOS, Wyatt) under the same conditions as used in our previous study.[25] Size distributions were calculated by the Astra software 4.90 (Wyatt) using the particle mode and assuming compact spheres. Characteristic diameters (D10, D50, and D90) were obtained from cumulative size distributions. All three nanoparticle batches (Table 1) were diluted with purified, filtered (0.2 μm) water (concentration, 1 mg/mL). The unloaded nanoparticles (1 mg/mL) were also dispersed in purified water and water supplemented with 10% and 50% FBS, respectively. All samples were measured with purified water (preserved and 0.2 μm filtered) as carrier liquid in triplicate, and results are given as an average with standard deviation. The accuracy of the AF4/MALLS separation system was routinely checked using a mixture of 50, 100, 200, and 300 nm polystyrene standard nanoparticles.[31]

Cell Culture for Confocal Microscopy. Human colon carcinoma cells (HT29) and human ovarian carcinoma cells (A2780) were cultivated as monolayers on round cover glasses with 80,000 HT29 or 85,000 A2780 cells per cm^2. Both cell lines were seeded and incubated in RPMI 1640 medium supplemented with 10% fetal bovine serum and 1% streptomycin/penicillin at 37 °C, 95% humidity, and 5% carbon dioxide. After 24 h the medium was removed and each of three round cover glasses with cells were incubated for 24 h with either unloaded, DiR-loaded nanoparticles (batch A, Table 1), or pure dispersion medium. A second series of each of three round cover glasses with cells were equally handled but stained additionally with DiO (Vybrant standard procedure) to visualize the cell membranes next to nanoparticles. After 24 h of incubation, the medium was removed and the cells were fixed with formalin in PBS (2% v/v) for 20 min at 37 °C. After washing the cells with PBS for three times, they were immediately imaged in a confocal microscope.

Confocal Microscopic Analysis. The LSM 710, a flexible confocal microscope (Zeiss, Germany), allows studying the cellular uptake of nanoparticles as well as of *ex vivo* excised tissues. The microscope was equipped with 40× or 63× Plan Apo oil immersion objectives. The DiR was excited with a 633 nm laser. Emitted fluorescence light was detected from 650 nm to the upper detection limit. The excitation of DsRed2, a red fluorescent protein, was carried out using the 514 nm laser. The 458 nm laser was used to excite DiO. Images were acquired in a sequential scan mode and processed using the ZEN software (Zeiss, Germany). To image the *ex vivo* samples the tumor tissue was excised and cut into small panels (thickness approximately 0.5 mm) by a racer plate. Afterward the tissue was slightly pressed between two cover glasses and immediately viewed with the LSM 710.

Animal Models and Nanoparticle Injection. Nanoparticle accumulation studies were preformed in male NMRI-nu (nu/nu) mice from JANVIER SAS in Le Genest Saint Isle, France. All experiments complied with the standards for use of animal subjects as stated in the guideline from the animal care and use committee of Saxony Anhalt. Aqueous nanoparticle dispersions (6 milligram nanoparticles per millliter) were prepared by redispersing adequate amounts of the freeze-dried nanoparticles (stabilized with 5% sucrose) in purified water containing 2.25% sorbitol to adjust tonicity. A 100 μL portion of the dispersion was slowly i.v. injected into the tail vein of non-narcotized mice using a 30 Gauge needle. During imaging the mice were narcotized and protected for cooling out.[25]

Xenograft Tumor Model and Application. HT29 and A2780 cells were maintained as monolayer cultures as given above. DsRed2 expressing HT29 cells were generated by lentiviral transduction according to the protocol described previously.[43]

After growing, 3×10^6 DsRed2 HT29 cells were subcutaneously injected into both flanks of nude mice. At a size of approximately 1.5 cm^3, 100 μL of batch A nanoparticles was injected and time dependent images were grabbed by fluorescence imaging.

For detailed size dependent tumor accumulation studies nonfluorescent s.c. xenograft tumors were established in 13 nude mice. A total of 3×10^6 HT29 cells were s.c. injected to the right flank of the mice and 3×10^6 cells of A2780 were injected into the left side. Body weights and tumor sizes were measured

twice a week. After the A2780 achieved a maximum tumor size of about 2 cm^3, the mice were separated into three groups (three mice each) and care was taken for a preferably homogeneous tumor size distribution. One untreated mouse was used as *in vivo* control and for further *ex vivo* microcopy studies. A 100 μL portion of each nanoparticle batch was injected in all three mice of the respective group: A, B, and C (named like the nanoparticle batch as in Table 1). The mice were imaged 24 h after injection and sacrificed, and the respective tumors were excised. The tumor was exactly determined with a caliper, and the tumor volume was calculated using the tumor dimensions of all 3 room directions assuming an elliptic tumor shape. All excised tumors were imaged as complete tissue and after slicing into 2 pieces.

***In Vivo* and *ex Vivo* Tumor Imaging.** *In vivo* and *ex vivo* fluorescence imaging experiments were preformed using the Maestro *in vivo* fluorescence imaging system (Cambridge Research and Instrumentation, United States).[25,44] The green filter set (503−555 nm excitation and 580 nm long-pass emission filters) was used to detect DsRed2 tumor cells. For nanoparticle imaging the NIR filter set with a 710−760 nm excitation and an 800 nm long-pass emission filter was used as described in our previous study.[25] To prevent fluorescence interferences between nanoparticle accumulations in the tumor and in the RES, the area of the liver was masked with a black plastic plate in selected imaging experiments. Recordings (cubes) were analyzed using *in vitro* DiR and cellular DsRed2 spectra as references, and the signal from an untreated mouse was set as background. The cubes were unmixed and segmented using these respective 2 or 3 spectra and saved as monochrome images. On the basis of these images, RGB (red green blue) pictures were generated allocating a respective color (DsRed2 in green and DiR in red) to the spectra. The generated grayscale images were also intensity-weighted illustrated.[25]

For *ex vivo* analysis the mice were sacrificed using carbon dioxide 24 h after injection of the nanoparticles (48 h in the case of DsRed2 expressing HT29 experiments). The excised tumors and organs (liver and spleen) were imaged with the Maestro *in vivo* imaging system using the same parameters as in the *in vivo* study. To ensure reproducible conditions the organs (liver and spleen) were placed in a 24 holes well-plate. An area of interest (ROI) in the size of the well-plate hole was generated. Total and maximum intensities of all pixels in the ROI were measured and correlated to the respective exposure times by the software. To exclude intensity variations due to different initial dye concentrations and intensities between the nanoparticle batches, a previously described correction method was applied.[25] The total signal (correlated to the exposure time) was divided through the *in vitro* emission peak maximum which was determined prior to the *in vivo* measurements. The *ex vivo* total and maximum intensity signals of the nanoparticle accumulation in the tumor tissues were furthermore divided through the *ex vivo* determined tumor size (volume of an ellipsoid, based on three room directions). All graphs are normalized to 100% related to the highest result. Excised tumors were fixed with 4% formalin for 1 week and afterward embedded in paraffin. Resulted blocks were sliced (4 nm), dewaxed, and stained with hematoxylin and eosin (H&E). Light microscopic images of the stained tissues were obtained using a Zeiss Axiolab microscope (Zeiss, Germany).

Acknowledgment. We thank Jürgen Vogel and Marcus Niepel for supporting the confocal microscopic measurements. Mr Jörg Tessmar is acknowledged for the discussions during polymer synthesis and nanoparticle preparation. We thank also Martina Hennicke and Constanze Gottschalk for the animal care. The *in vivo* studies were partly supported by the Federal State of Saxonia Anhalt (FKZ 3646A/0907) and the confocal microscopy studies by the Deutsche Forschungs-gemeinschaft (LSM: INST 271/250-1).

REFERENCES AND NOTES

1. Lipinski, C. A.; Lombardo, F.; Dominy, B. W.; Feeney, P. J. Experimental and Computational Approaches to estimate Solubility and Permeability in Drug Discovery and Development Settings. *Adv. Drug Delivery Rev.* **1997**, *23*, 3–25.
2. Milne, G. Pharmaceutical Productivity—The Imperative for New Paradigms. *Annu. Rep. Med. Chem.* **2003**, *38*, 383–396.
3. Yokogawa, K.; Nakashima, E.; Ishizaki, J.; Maeda, H.; Nagano, T.; Ichimura, F. Relationships in the Structure Tissue Distribution of Basic Drugs in the Rabbit. *Pharm. Res.* **1990**, *7*, 691–696.
4. Feng, S. S. New-Concept Chemotherapy by Nanoparticles of Biodegradable Polymers: Where are we now?. *Nanomedicine* **2006**, *1*, 297–309.
5. Musumeci, T.; Ventura, C. A.; Giannone, I.; Ruozi, B.; Montenegro, L.; Pignatello, R.; Puglisi, G. PLA/PLGA Nanoparticles for Sustained Release of Docetaxel. *Int. J. Pharm.* **2006**, *325*, 172–179.
6. Xing, J.; Zhang, D. R.; Tan, T. W. Studies on the Oridonin-loaded Poly(D,L-lactic acid) Nanoparticles *in Vitro* and *in Vivo*. *Int. J. Biol. Macromol.* **2007**, *40*, 153–158.
7. Brigger, I.; Dubernet, C.; Couvreur, P. Nanoparticles in Cancer Therapy and Diagnosis. *Adv. Drug Delivery Rev.* **2002**, *54*, 631–651.
8. Dunn, S. E.; Coombes, A. G. A.; Garnett, M. C.; Davis, S. S.; Davies, M. C.; Illum, L. *In Vitro* Cell Interaction and *in Vivo* Biodistribution of Poly(lactide-*co*-glycolide) Nanospheres Surface Modified by Poloxamer and Poloxamine Copolymers. *J. Controlled Release* **1997**, *44*, 65–76.
9. Moghimi, S. M.; Hunter, A. C.; Murray, J. C. Long-Circulating and Target-Specific Nanoparticles: Theory to Practice. *Pharmacol. Rev.* **2001**, *53*, 283–318.
10. Maeda, H. Tumor-Selective Delivery of Macromolecular Drugs *via* the EPR Effect: Background and Future Prospects. *Bioconjugate Chem.* **2010**, *21*, 797–802.
11. Yuan, F.; Dellian, M.; Fukumura, D.; Leunig, M.; Berk, D. A.; Torchilin, V. P.; Jain, R. K. Vascular-Permeability in a Human Tumor Xenograft—Molecular-Size Dependence and Cutoff Size. *Cancer Res.* **1995**, *55*, 3752–3756.
12. Hobbs, S. K.; Monsky, W. L.; Yuan, F.; Roberts, W. G.; Griffith, L.; Torchilin, V. P.; Jain, R. K. Regulation of Transport Pathways in Tumor Vessels: Role of Tumor Type and Microenvironment. *Proc. Natl. Acad. Sci. U.S.A.* **1998**, *95*, 4607–4612.
13. Moghimi, S. M.; Porter, C. J. H.; Muir, I. S.; Illum, L.; Davis, S. S. Non-phagocytic Uptake of Intravenously Injected Microspheres in Rat Spleen—Influence of Particle-Size and Hydrophilic Coating. *Biochem. Biophys. Res. Commun.* **1991**, *177*, 861–866.
14. Moghimi, S. M. Mechanisms of Splenic Clearance of Blood-Cells and Particles—Towards Development of New Splenotropic Agents. *Adv. Drug Delivery Rev.* **1995**, *17*, 103–115.
15. Nakaoka, R.; Tabata, Y.; Yamaoka, T.; Ikada, Y. Prolongation of the Serum Half-Life Period of Superoxide Dismutase by Poly(ethylene glycol) Modification. *J. Controlled Release* **1997**, *46*, 253–261.
16. Lammers, T.; Kuhnlein, R.; Kissel, M.; Subr, V.; Etrych, T.; Pola, R.; Pechar, M.; Ulbrich, K.; Storm, G.; Huber, P.; Peschke, P. Effect of Physicochemical Modification on the Biodistribution and Tumor Accumulation of HPMA Copolymers. *J. Controlled Release* **2005**, *110*, 103–118.
17. Lammers, T.; Subr, V.; Ulbrich, K.; Hennink, W. E.; Storm, G.; Kiessling, F. Polymeric Nanomedicines for Image-Guided Drug Delivery and Tumor-Targeted Combination Therapy. *Nano Today* **2010**, *5*, 197–212.
18. Seymour, L. W.; Miyamoto, Y.; Maeda, H.; Brereton, M.; Strohalm, J.; Ulbrich, K.; Duncan, R. Influence of Molecular-Weight on Passive Tumor Accumulation of a Soluble Macromolecular Drug. Carrier. *Eur. J. Cancer* **1995**, *31A*, 766–770.
19. Litzinger, D. C.; Buiting, A. M. J.; Vanrooijen, N.; Huang, L. Effect of Liposome Size on the Circulation Time and Intraorgan Distribution of Amphipathic Poly(Ethylene Glycol)-Containing Liposomes. *Biochim. Biophys. Acta, Biomembr.* **1994**, *1190*, 99–107.
20. Liu, D. X.; Mori, A.; Huang, L. Role of Liposome Size and RES Blockade in Controlling Biodistribution and Tumor Uptake

of Gm1-Containing Liposomes. *Biochim. Biophys. Acta* **1992**, *1104*, 95–101.
21. Storm, G.; Belliot, S. O.; Daemen, T.; Lasic, D. D. Surface Modification of Nanoparticles to Oppose Uptake by the Mononuclear Phagocyte System. *Adv. Drug Delivery Rev.* **1995**, *17*, 31–48.
22. Beletsi, A.; Panagi, Z.; Avgoustakis, K. Biodistribution Properties of Nanoparticles Based on Mixtures of PLGA with PLGA-PEG Diblock Copolymers. *Int. J. Pharm.* **2005**, *298*, 233–241.
23. Pegaz, B.; Debefve, E.; Ballini, J. P.; Konan-Kouakou, Y. N.; van den Bergh, H. Effect of Nanoparticle Size on the Extravasation and the Photothrombic Activity of Meso (*p*-Tetracarboxyphenyl) Porphyrin. *J. Photochem. Photobiol. B* **2006**, *85*, 216–222.
24. Gaumet, M.; Vargas, A.; Gurny, R.; Delie, F. Nanoparticles for Drug Delivery: The Need for Precision in Reporting Particle Size Parameters. *Eur. J. Pharm. Biopharm.* **2008**, *69*, 1–9.
25. Schädlich, A.; Rose, C.; Kuntsche, J.; Caysa, H.; Mueller, T.; Göpferich, A.; Mäder, K. How Stealthy Are PEG–PLA Nanoparticles? An NIR *in Vivo* Study Combined with Detailed Size Measurements. *Pharm. Res.* **2011**, *28*, 1995–2007.
26. Shuhendler, A. J.; Prasad, P.; Chan, H. K. C.; Gordijo, C. R.; Soroushian, B.; Kolios, M.; Yu, K.; O'Brien, P. J.; Rauth, A. M.; Wu, X. Y. Hybrid Quantum Dot-Fatty Ester Stealth Nanoparticles: Toward Clinically Relevant *in Vivo* Optical Imaging of Deep Tissue. *ACS Nano* **2011**, *5*, 1958–1966.
27. Jiang, Y. J.; Schädlich, A.; Amado, E.; Weis, C.; Odermatt, E.; Mäder, K.; Kressler, J. *In-Vivo* Studies on Intraperitoneally Administrated Poly(vinyl alcohol). *J. Biomed. Mater. Res. Part B* **2010**, *93B*, 275–284.
28. Rose, C. Particulate Systems for Fluorescence Imaging and Drug Delivery. Thesis, University of Regensburg, Germany, December, 2010.
29. Coffin, M. D.; Mcginity, J. W. Biodegradable Pseudolatexes—The Chemical-Stability of Poly(D,L-Lactide) and Poly(ε-caprolactone) Nanoparticles in Aqueous-Media. *Pharm. Res.* **1992**, *9*, 200–205.
30. Dunne, M.; Corrigan, O. I.; Ramtoola, Z. Influence of Particle Size and Dissolution Conditions on the Degradation Properties of Polylactide-*co*-glycolide Particles. *Biomaterials* **2000**, *21*, 1659–1668.
31. Kuntsche, J.; Klaus, K.; Steiniger, F. Size Determinations of Colloidal Fat Emulsions: A Comparative Study. *J Biomed Nanotechnol* **2009**, *5*, 384–395.
32. Lohrke, J.; Briel, A.; Mader, K. Characterization of Superparamagnetic Iron Oxide Nanoparticles by Asymmetrical Flow-Field–Flow-Fractionation. *Nanomedicine* **2008**, *3*, 437–452.
33. Desai, M. P.; Labhasetwar, V.; Walter, E.; Levy, R. J.; Amidon, G. L. The Mechanism of Uptake of Biodegradable Microparticles in $CaCo_2$ Cells Is Size Dependent. *Pharm. Res.* **1997**, *14*, 1568–1573.
34. Gref, R.; Luck, M.; Quellec, P.; Marchand, M.; Dellacherie, E.; Harnisch, S.; Blunk, T.; Muller, R. H. 'Stealth' Corona–Core Nanoparticles Surface Modified by Polyethylene Glycol (PEG): Influences of the Corona (PEG Chain Length and Surface Density) and of the Core Composition on Phagocytic Uptake and Plasma Protein Adsorption. *Colloid Surface B* **2000**, *18*, 301–313.
35. Fang, J.; Nakamura, H.; Maeda, H. The EPR Effect: Unique Features of Tumor Blood Vessels for Drug Delivery, Factors Involved, and Limitations and Augmentation of the Effect. *Adv. Drug Delivery Rev.* **2011**, *63*, 136–151.
36. Seki, T.; Fang, J.; Maeda, H. Enhanced Delivery of Macromolecular Antitumor Drugs to Tumors by Nitroglycerin Application. *Cancer Sci.* **2009**, *100*, 2426–2430.
37. Caysa, H.; Metz, H.; Mäder, K.; Mueller, T. Application of Benchtop-Magnetic Resonance Imaging in a Nude Mouse Tumor Model. *J. Exp. Clin. Cancer Res.* **2011**, *30*, 69.
38. Minko, T.; Kopeckova, P.; Kopecek, J. Efficacy of the Chemotherapeutic Action of HPMA Copolymer-Bound Doxorubicin in a Solid Tumor Model of Ovarian Carcinoma. *Int. J. Cancer* **2000**, *86*, 108–117.
39. Buadu, L. D.; Murakami, J.; Murayama, S.; Hashiguchi, N.; Sakai, S.; Toyoshima, S.; Masuda, T.; Kuroki, S.; Ohno, S. Patterns of Peripheral Enhancement in Breast Masses: Correlation of Findings on Contrast Medium Enhanced MRI with Histologic Features and Tumor Angiogenesis. *J. Comput. Assist. Tomogr.* **1997**, *21*, 421–430.
40. Schmid, S. A.; Dietrich, A.; Schulte, S.; Gaumann, A.; Kunz-Schughart, L. A. Fibroblastic Reaction and Vascular Maturation in Human Colon Cancers. *Int. J. Radiat. Biol.* **2009**, *85*, 1013–1025.
41. Jain, R. K. Transport of Molecules, Particles, and Cells in Solid Tumors. *Annu. Rev. Biomed. Eng.* **1999**, *1*, 241–263.
42. Minko, T.; Kopeckova, P.; Pozharov, V.; Jensen, K. D.; Kopecek, J. The Influence of Cytotoxicity of Macromolecules and of VEGF Gene Modulated Vascular Permeability on the Enhanced Permeability and Retention Effect in Resistant Solid Tumors. *Pharm. Res.* **2000**, *17*, 505–514.
43. Luetzkendorf, J.; Mueller, L. P.; Mueller, T.; Caysa, H.; Nerger, K.; Schmoll, H. J. Growth Inhibition of Colorectal Carcinoma by Lentiviral TRAIL-Transgenic Human Mesenchymal Stem Cells Requires Their Substantial Intratumoral Presence. *J. Cell. Mol. Med.* **2010**, *14*, 2292–2304.
44. Kobayashi, H.; Koyama, Y.; Barrett, T.; Hama, Y.; Regino, C. A. S.; Shin, I. S.; Jang, B. S.; Le, N.; Paik, C. H.; Choyke, P. L.; Urano, Y. Multimodal Nanoprobes for Radionuclide and Five-Color Near-Infrared Optical Lymphatic Imaging. *ACS Nano* **2007**, *1*, 258–264.